# Revised Algorithm Theoretical Basis Document (ATBD) for

# Rain Detection and Measurement from Megha-Tropiques Microwave Sounder – SAPHIR

Atul Kumar Varma, D N Piyush, R M Gairola and B S Gohil

Geophysical Parameters Retrieval Division
Atmospheric and Oceanic Sciences Group
Space Applications Centre (ISRO)
Ahmedabad 380015, India

February 2015

# Document Control and Data Sheet

| 1 | Date | February 24, 2015 |
|---|---|---|
| 2. | Title: | Revised Algorithm Theoretical Basis Document (ATBD): Rain Detection and Measurement from Megha-Tropiques Microwave Sounder – SAPHIR |
| 3. | Version | 1.1 |
| 4. | Document No. | SAC/EPSA/AOSG/SR/01/2015 |
| 5. | Type of Report: | scientific Note |
| 6. | No. of Pages: | 27 (excluding title page) |
| 7. | Author: | Atul K Varma, D N Piyush. R M Gairola and B S Gohil |
| 8. | Originating unit: | GRD/AOSG/EPSA/SAC, Ahmedabad. |
| 9. | Abstract: | Megha-Tropiques satellite carries onboard a microwave sounder, SAPHIR, and a microwave radiometer, MADRAS, along with two other instruments. Due to currently non-functioning of MADRAS, the possibility of detection and estimation of rain from SAPHIR is explored. The SAPHIR operates in 6 frequencies ranging from $183.31\pm0.2$ to $183.31\pm11$ GHz which are close to water vapor absorption line at 183.31 GHz. In the first step, an examination of the rain effect on SAPHIR channels is carried out, and the results showed them to be sensitive to the rain. In the second step, a rain identification algorithm is attempted, which is based on average rain probability ($P_R$) measured at SAPHIR channels. The effect of false alarm and missing rain is examined and it is found that missing rain over land and ocean is < 0.9 mm/h and 0.13 mm/h with standard deviation of 0.70 mm/h and 0.54 mm/h, respectively, and rain due to false alarm over both land and oceans is < 0.9 mm/h. In the third step, a nonlinear rain retrieval algorithm is proposed for rain affected pixels, which explains a correlation of 0.70 and rmse of 0.81 mm/h. When rain identification and retrieval algorithms are applied together, it explains a correlation of 0.68 and rmse of 0.45 mm/h on instantaneous basis. Comparison of rain from SAPHIR with TRMM-3B42 on monthly basis indicates a correlation of 0.84 and rms difference of 0.09 mm/h. In this report step-by-step procedure in given to make this algorithm operational. |
| 10. | Classification: | Unrestricted |
| 11. | Distribution: | All concerned |

# Rain Detection and Measurement from Megha-Tropiques Microwave Sounder – SAPHIR

## 1. Introduction:

In order to study the tropical convective systems and their dominance in defining the energy and water cycle in the atmosphere, several atmospheric variables like precipitation, surface evaporation, net radiation at the top of the atmosphere, vertical profile of temperature and humidity, etc, play a crucial role, and hence it is imperative to measure these variables simultaneously. This is planned to be achieved through a joint Indo-French collaborative Megha-Tropiques (MT) satellite mission. Megha-Tropiques satellite was launched on 12 October 2011, and is purposely designed to study the convective systems, water cycles and energy exchanges in the tropical atmosphere through a host of onboard instruments such as Microwave Analysis and Detection of Rain and Atmospheric Structures (MADRAS), Sondeur Atmosphérique du Profil d'Humidité Intertropical par Radiométrie (SAPHIR), Scanner for Radiation Budget (ScaRaB) and Radio Occultation Sensor for Atmosphere (ROSA). To facilitate frequent observations over the tropics, the Megha-Tropiques is placed in a low inclination orbit (20º) at 867 km altitude that provides the coverage over the global tropical region with 14 orbits a day and 7 days of repeat cycle.

The MADRAS onboard MT is a five-frequency, nine-channel, self-calibrating, microwave radiometer that sweeps a swath of ~1700 km in a conical scanning with local incidence angle of 53.5º on the surface of the Earth. The specifications of MADRAS are provided in Table 1. MADRAS observations are used to operationally derive Total Precipitable Water (TPW), Cloud Liquid Water (CLW), and Ocean Surface Wind Speed (OWS) over oceans, and rain over land and oceans using radiative transfer based approach developed by Varma et al. (2011) and a scattering index based approach developed by Gairola et al. (2011). The SAPHIR is a six-channel microwave sounder that carries out cross track scanning within ±50º on both sides of the nadir and thereby providing variable incidence angle and variable pixel size over a swath of ~1700 km. The specifications of SAPHIR are given in Table 2. The SAPHIR that operates at frequencies around water vapor resonance line at 183.31 GHz is designed to provide clear-sky profiles of atmospheric humidity. Frequencies near 183.31 GHz show very high atmospheric absorption and the emitted radiations from the environment reaching to the satellite are dominated by contribution from broad atmospheric layers whose thickness and mean altitude vary with operating frequency as well as with humidity and temperature in the atmosphere. Using observations from SAPHIR channels, algorithms are developed to operationally derive the Atmospheric Humidity profiles (Gohil et al., 2013, Mathur et al., 2013).

Rain is an important atmospheric parameter and is most fundamental to achieve science objectives of the Megha-Tropiques mission. Keeping this is view, the MADRAS onboard MT mission is specifically designed to measure the rain. However, after few months of successful operation, some anomaly was observed in the MADRAS

observations due to a suspected electrical interference which resulted in to random channel mixing. A methodology is worked out by the CNES and ISRO Project teams for realignment of the data. With this additional processing, a significant amount of data is recovered. However, another serious anomaly observed in MADARS scan mechanism and the MADRAS instrument is declared non-operational on 26 January 2013 (please see, http://smsc.cnes.fr/MEGHAT/GP_actualites.htm). In view of these facts, we herein make an attempt to measure rain from SAPHIR observations which may help fulfilling science objectives of the MT mission in the absence of the MADRAS observations.

For rain measurement, passive microwave radiometers operating below 90 GHz frequency (e.g., TMI, SSM/I, AMSR-E, MADRAS, etc.) are commonly used. Frequencies above 90 GHz are available on number of sensors like SSMIS, SSM/T 2 (Special Sensor Microwave Temperature 2) onboard DMSP satellite, AMSU (Advance Microwave Sounder Unit) onboard Aqua and NOAA 17, and MADRAS and SAPHIR onboard MT. The frequencies above 90 GHz are commonly used for studying the cloud properties (e.g., Liu and Curry, 1990, Weng, 2003, etc.). Hong et al. (2005) have studied the sensitivity of the microwave brightness temperatures to hydrometeors at 89-190 GHz frequencies, and found that frequencies near water vapor absorption band at 183.31 GHz (e.g., AMSU-B channels) are nearly independent of surface emissivity because of atmospheric opacity at these frequencies. This finding allows development of retrieval algorithms for rain/cloud and other atmospheric parameters independent of the underlying surface type. Several other researchers (e.g., Muller et al., 1994; Hong et al., 2005) have also studied the effect of cloud ice and precipitation on AMSU-B water vapor channels. A depression in the satellite measured brightness temperature at frequencies near water vapor absorption line (183.31 GHz) is resulted from the hydrometeors on the top of the cloud, and the depression increases for frequencies away from the water vapor absorption line (Burns et al., 1997). Thus for SAPHIR, we expect higher depression for 183.31±11 GHz channel. Bennartz and Bauer (2003) have studied the sensitivity of the frequencies near 183.31 GHz water vapor absorption line to ice particle scattering in different environmental conditions, and reported little sensitivity to precipitating clouds below 8 km of altitude, which they attributed to the peaking of the weighting functions at higher altitudes.  The study by Bennartz and Bauer (2003) was conducted for middle and higher latitude conditions and for 183±7, 183±3, 183±1 GHz channels, we, however, expect a higher sensitivity of SAPHIR 183±11 GHz channel to precipitating clouds.

SAPHIR on MT collects microwave radiances from the environment at 6 channels around water vapor absorption band at 183.3 GHz. These channels are referred as S1, S2, S3, S4, S5 and S6 with central operating frequency of 183.31±0.2 GHz, 183.31±1.1 GHz, 183.31±2.8 GHz, 183.31±4.2 GHz, 183.31±6.8 GHz, and 183.31±11.0 GHz. The SAPHIR sweeps a swath of ~1700 km while carrying out cross-track scanning of ±50º on both sides of the nadir. The SAPHIR swath dataset comprises of 182 pixels with 91 pixels on both sides of the nadir. It provides variable local incidence angle along the swath at the surface of the Earth. The spatial resolution also varies along the swath from 10 km at nadir to about 22 km at pixel locations 1 and 182.  In the present study

we have used SAPHIR swath observations of period from March - May 2013 and also of Phaillin Cyclone over the Bay of Bengal on 11 October 2013.

In this report, we make an attempt to detect and determine precipitation amount using SAPHIR frequencies near water vapor absorption line at 183.31 GHz (Table-2). The rain measured from SAPHIR may provide an alternate and independent set of measurements to fulfill the MT Science objectives, especially in view of absence of MADRAS measurements.

## 2. Rain Detection

Rain identification algorithm is an integral part of any satellite passive microwave based rain retrieval algorithm. At microwave frequencies (say, from 6 GHz to 190 GHz) variations in the surface emissivity, surface and atmospheric temperature, water vapor, cloud liquid water or wind speed may produce the brightness temperature (Tb) variations of the same order as that due to rain rates. Apart from that the uncertainties observed in the brightness temperature versus rain rate relationship due to horizontal and vertical rain variability within satellite IFOV makes it extremely difficult to differentiate low rain rates from the background field (Varma et al., 2004). The rain identification over the land is even more complex due to strong and highly varying emissivity, especially at low microwave frequencies. Varma and Pal (2012) have provided a detailed account of the problem of precipitation detection by passive microwave measurements.

Here, we intend to develop a rain identification algorithm using SAPHIR brightness temperature measurements. Because of high atmospheric opacity at frequencies near the water vapor absorption line (183.31 GHz), the measurements are nearly independent of the surface emissivity (Hong et al., 2005), but the cloud structure over land is different than the oceans (Kawamoto and Suzuki, 2013, Varma and Liu, 2006); Clouds over land usually develop much deeper than that over the oceans, and therefore, they may exhibit different brightness temperature depression for a given rain rate. Furthermore, unlike passive microwave radiometers with conical scan mechanism that are traditionally used for rain measurement, like SSM/I, TMI, MADRAS, etc., the SAPHIR incidence angle at each scan position differs and that has to be incorporated in any retrieval algorithm. Ideally, the pixels that are equidistant from the nadir on a scan line should have same incidence angle. But such pixels may still have asymmetry resulting from radio frequency interference problem of the instrument (Buehler et al., 2005). Thus we have attempted the development of the algorithm by considering all 182 pixels independently over land and oceans.

In order to develop rain identification algorithm, we use concurrent observations from SAPHIR and Tropical Rainfall Measuring Mission (TRMM)- Precipitation Radar PR. Apart from PR, TRMM also carried onboard a microwave radiometer which is referred as Microwave Radiometer (TMI). Rain rates are provided by both TMI and PR. TMI operates at 10.65, 19.35, 21.3, 37.0, and 85.5 GHz with all frequencies, except 21.3 GHz (only V) received radiation in both vertical and horizontal polarizations. TRMM is a

low orbiting satellite, which provides coverage between about 36º S and 36º N latitudes. The PR scans ± 17° from the nadir with 49 positions result in a 215 km swath, with a spatial resolution of 4.3 km. In August 2001 the TRMM orbit was raised from 350 to 403 km, and that resulted to extended swath of 247 km and spatial resolution of ~5 km. In the present study, we use precipitation radar measurements taken from TRMM standard swath product 2A25, which contains the rainfall rates from surface to 20 km altitude with 250 m vertical resolution. We have also taken surface rain rates from TMI standard data product 2A12. The TRMM sensor package has been described by Kummerow et al. (1998), and PR rain measurement algorithm is provided by Awaka et al. (1997). The TRMM sensor package has been described by Kummerow et al. (1998), and PR rain measurement algorithm is provided by Awaka et al. (1997).

The dataset of PR-SAPHIR concurrent observations is prepared by collocating SAPHIR and PR observations over space and time. We assume a circular foot print of SAPHIR of diameter 10 km at the nadir and that varies linearly to 22 km at the beginning and end of a scan line (i.e., pixel # 1 and 182). We find all the PR observations that fall on a SAPHIR footprint within 10 minutes of time difference and calculate the weighted average surface rain rate from PR observations. The weight is varied commensurating for an assumed isotropic antenna gain pattern over the footprint. This way we generate a collocated SAPHIR-PR dataset for March 2013 for further analysis. We refer it as training dataset in the succeeding part of this report. Given the temporal variability of the precipitation (Piyush et al., 2012) and non-circular footprint of the SAPHIR away from nadir, collocation of two datasets in spatial and temporal domain is not the perfact, yet keeps the procedure of collocation simple while providing a large collocated dataset of about 1.7 million observations over the ocean and 0.7 million over land. The rain identification and retrieval scheme have been performed separately for the land and oceans. We further divided dataset into rainy and non-rainy sets for 182 swath positions of the SAPHIR. We examine the probability distribution (PDF) of brightness temperatures measured at all 6 channels of SAPHIR for rainy and non-rainy conditions for all scan locations. Figure 1 (a) to (f) show plots of PDFs of SAPHIR brightness temperatures for channel S1 and S6 for a typical scan position # 45 for rainy and non-rainy conditions over the oceans. There do exist similar PDFs for other pixel locations over the oceans and land. The PDF of the brightness temperatures for rainy cases is shown as line joining open circles and that for non-rainy cases is shown as line joining solid circles. It may be observed that there is large overlap of PDFs of brightness temperatures from all the channels for rainy and non-rainy cases, and thus making it difficult to identify a threshold value of brightness temperature for clearly demarcating rainy and non-rainy conditions.  Despite of having large overlap area between PDFs of rainy and non-rainy cases, the Fig. 1 shows clear and distinct peaks of PDFs for two cases in all the 6 channels of SAPHIR, which suggest some tangible sensitivity of the brightness temperatures to rain.  Figure 1 shows PDFs of brightness temperatures for a typical scan position over the oceans, there, however, exists similar qualitative behavior of PDFs of brightness temperatures for rainy and non-rainy cases at other scan positions over land and oceans as well. We thus take advantage of sensitivity of all the six SAPHIR channels towards rainfall as provided by the probability distribution of brightness temperatures for rainy and non-rain cases, separately for all 182 pixel

locations (please note that Fig. 1 (a) – (f) is just an example for pixel location # 45 over the oceans), and calculate the average probability of a given pixel as rainy ($P_R$) and non-rainy ($P_{NR}$). We normalize the $P_R$ and $P_{NR}$ to make their sum unity. Now, we examine the $P_R$ (or $P_{NR}$) by plotting distribution of $P_R$ from all pixel locations calculated separately from rainy and non-rainy SAPHIR-PR collocated training datasets (Fig. 2a) for ocean and Fig (2b) for the land. The distribution of $P_R$ from non-rainy dataset is shown as line joining open circles and that for rainy dataset is shown as line joining open triangles. We still find a large overlap between two plots in Fig.2 (a), (b). However, we notice a long tail in the distribution of $P_R$ associated with non-rainy dataset and a double peak in the distribution associated with rainy dataset. Thus it is possible that in the SAPHIR-PR collocated dataset a large number of pixels which are considered as non-raining are actually rainy and vice versa. This could be possible as collocation in space and time is not perfect as discussed above. There may also be some problem in the collocation due to other reasons like sensitivity of PR (~0.7 mm/h) (anonymous, 2011), angle of observation, etc. Thus, we do not take $P_R$=0.5 as the threshold value to identify rain/no-rain and a more appropriate value of the $P_R$ threshold is worked out. We examined different threshold values of $P_R$ and tried to identify most appropriate value of $P_R$ which is optimized for minimal error in the identification of rain/no-rain. This procedure led us to find a $P_R$ value of 0.6 as most appropriate value for ocean and 0.63 for land. According to Fig. 2 (a), the $P_R$ threshold of 0.6 results in about 9% false rain pixels from non-rainy pixels and 34% missing rain from rainy pixels over oceans, whereas, over land with $P_R$ = 0.63 there is about 7% false rain pixels from non-rainy and 27% missing rain from rainy pixels. We further examine how these wrongly identified pixels with $P_R$ thresholds would have likely ramification on the rain identification and measurement. Figure 3 (a) and (b) shows the average rain with vertical bars of Standard Deviation (SD) as a function of $P_R$ from the rainy dataset of ocean and land, respectively. As expected the average rain is small in lower values of $P_R$, and increases as we go to higher values of $P_R$. Over oceans, the average rain at $P_R$ = 0.6 is 0.13 mm/h with SD of 0.54 mm/h. We follow the same procedure over land and find that average rain at $P_R$ = 0.63 is 0.09 mm/h with SD of 0.70 mm/h. Thus, the rainy points that are classified as non-rainy would contribute only to very low rain regime (say, < ~0.7 mm/h). We further examine the non-raining point that turn raining with the $P_R$ thresholds. Figure 4 shows the cumulative probability distribution of rain rates for such pixels. The rain rate is calculated from an algorithm discussed in the next section. From the Fig. 4, we find that for oceans (open triangles) about 80% of the non-raining pixels that give false rain produce an average rain of less than 0.15 mm/h. About 95% of such pixels produce average rain of less than 0.35 mm/h, whereas for land about 52 % of the non-raining pixels give an average rain of 0.15 mm/h, and 95 % of such pixels produce an average rain less than 0.65 mm/h and none of them yield average rain of more than 0.95 mm/h. Thus, with the $P_R$ based rain/no-rain threshold, the rainy pixels that are classified as producing missing-rain and the non-rainy pixels that are classified as producing false-rain has effect only in the low rain regime (i.e., < 1 mm/h). Given the errors in the rain estimation by the microwave radiometers (Varma et al., 2010, Varma and Pal, 2012), and the error involved in the spatial-temporal collocation of the SAPHIR-PR dataset, this error in the rain identification can be considered as insignificant. Hence, with a $P_R$ threshold of 0.6 and 0.63 as discussed above, we generate rain/no-rain map from

SAPHIR and also from TRMM 3B42 standard dataset. Figure 5 shows rain/no-rain map for a typical day of 11 May 2013. Due to rain identification problem in very low rain regime, we have deliberately avoided low rain rates of < 0.25 mm/h. Again the SAPHIR rain is determined using the rain retrieval algorithm discussed in the next section. The Fig. 5 shows that rain area by SAPHIR matches fairly well with that from 3B42.

## 3. Rain Retrieval

In the previous section, rain identification in SAPHIR observations is discussed. In this section, we make an attempt to retrieve the rain. For development of the retrieval algorithm, we first tried to examine the expected behavior of SAPHIR frequency channels with rain. For that we use radiative transfer simulations, we simulate brightness temperatures using a scattering based microwave radiative transfer model (MWRT) developed by Liu (1998) for all the six channels of SAPHIR. In these model simulations, we use a standard tropical atmospheric profile over calm oceans with surface temperature of 300 K. Figure 6 (a) shows plot of the brightness temperature versus rain rate for a typical scan position of for all the six channels of SAPHIR. Here, it may be observed that channel 1 (S1) i.e., at 183.31±0.2 GHz, exhibits the minimum slope and is thus least affected, and channel 6 (S6) i.e., at 183.31±11.0 GHz, exhibits the maximum slope and is thus most affected by the rain This is in agreement with many previous studies (e.g. Eymard et al., 2001, Bennartz and Bauer, 2003, etc.). Next, we have taken the difference of these two channels and tried to analyze the behavior against the rain rate. Taking this into consideration, we try to observe the relation of brightness temperature difference of least and most affected channels with rain rate. Fig 6 (b) shows the variation of brightness temperature difference ($\Delta T_b$) with rain rate (mm/h), which is exponential in nature. We follow the same procedure on land also, and the exponential relation holds well over land too, with different pairs of coefficients. A similar relationship is observed for all other scan locations over land and oceans.

For rain retrieval algorithm, we use the SAPHIR and PR collocated dataset as referred in the previous section. First, for each of the scan positions, we separate the data over land and ocean and then divided them further into two parts - rainy and no rainy. We, however, use only rainy pixels and referred this dataset as a training data set. As discussed above, from radiative transfer simulations, we find an exponential relationship between rain rate and the difference of brightness temperatures measured at S1 and S2. We thus use the following form of the equation for ocean and land and for each pixel location,

$$R = a + b * e^{c * \Delta T_b} \qquad (1)$$

Where, R is rain rate in (mm/h), a, b and c are regression coefficients. We calculate the values of a, b and c for separately over land and oceans and at each of the pixel locations. In order to define the accuracy of the rain estimation algorithm, we apply rain identification algorithm and the eq. (1) to the training dataset of collocated SAPHIR and PR observations of rainy pixels and calculate rain rate from SAPHIR observations at each pixel location and compared with the PR rain rates. This provides a correlation of

0.70, rms error of 0.81 mm/h and bias of 0.04 mm/h for total number of observations of about 0.94 million. When we consider all the collocated SAPHIR and PR observations from the training dataset comprising of rain as well as no rain observations, the correlation still remains 0.68 with an rms error of 0.45 mm/h, and bias of 0.01 mm/h for total number of 2.06 million observations. If this algorithm is used operationally, the SAPHIR observations subjected to the rain retrieval algorithm would not be pre-classified as rainy or non-rainy and hence the statistics provided in the latter case provides the algorithm accuracy. In order to test the algorithm with independent dataset, we have collocated SAPHIR and PR measurement for another one month of April 2013 by following the same procedure for collocation as done for training dataset. We refer this dataset as test dataset and apply the algorithm to the test dataset and compare the rain from SAPHIR with that from PR. With a test dataset we find a correlation of 0.58, rms error of 0.91 mm/h and bias of 0.07 mm/h for total number of observations of 2.3 million. These results are very encouraging given the high temporal variability of precipitation (Piyush et al., 2012) and possible imperfection in preparing collocated dataset of SAPHIR and PR as discussed earlier. These results appear to be more encouraging in view of similar comparison that we carried out between TMI and PR for a period of 10 days from 21-30 May 2009 that shows a correlation of 0.61, rms error of 2.23 mm/h, and bias of 0.1 mm/h for total number of observations of 1.88 million. It may be noted that PR and TMI are on the same orbiting platform with less than a minute of time difference between their observations, whereas we allowed 10 minutes of time difference between SAPHIR and PR observations.

Further, we have compared the monthly averaged rain rates from SAPHIR, TRMM-3B42 and SSMIS. Figure 7 (a), (b) and (c) shows the monthly gridded ($0.25^{o}$X$0.25^{o}$) maps of precipitation for the month of May 2013 from SAPHIR, TRMM-3B42 and SSMIS. Here we use SSMIS rain product (Hilburn and Wentz, 2008) which provides rain only over the oceans. As it can be seen there is a good qualitative comparison among three different rain products. The scatter plots of cross comparison among these three monthly maps is plotted in Fig. 8, which shows comparison between SAPHIR versus TRMM-3B42, SAPHIR versus SSMIS and SSMIS versus TRMM-3B42, respectively. The Fig. 8 (a) (b) and (c) shows the comparison over the land as well as the oceans, whereas other two Figs. 7 (d) and (e) shows a comparison over oceans only. The comparison between SAPHIR and TRMM-3B42 is most encouraging with a correlation coefficient of ~0.87 over ocean and 0.82 over land, when ocean and land both considered together correlation becomes 0.84 with rmse of 0.09 mm for 327743 valid points. On the other hand, the comparison of SSMIS monthly rain with monthly rain from SAPHIR and TRMM-3B42 shows a correlation of 0.69 and 0.65, respectively. Similar comparison of daily averaged rain from SAPHIR, TRMM-3B42 and SSMIS shows correlation of 0.65, 0.48 and 0.54, and rms difference of 0.31, 0.62, 0.56 mm/h, respectively. We have also tried to examine the distribution of daily averaged rain rates, for that we compared the Probability Distribution Function (PDF) of daily averaged rain over tropics from SAPHIR with TRMM-3B42 for a typical month of May, 2013 (Fig. 9). The Fig. 9 shows a good agreement of the PDF of the daily averaged rain from SAPHIR and 3B42.

In order to show a meaningful comparison of the quality of rain estimation using SAPHIR with that from TMI and PR, we make monthly average comparison of rain over land from SAPHIR with TMI and PR in 2.5°x2.5°, and comparison with the similar statistics between PR and TMI provided by Wang et al. (2009). They have provided comparison statistics of rain derived from TMI (2A12), PR (2A25) and Global Precipitation Climatology Centre (GPCC) (Rudolf, 1995). Based on 10 years of TRMM observations over land they have reported a correlation of 0.78 between 2A12 and 2A25 monthly mean rain rates. We have also compared SAPHIR monthly rain rates with TMI and PR for a typical month of November 2012 and found a correlation of 0.86 between SAPHIR and 2A12, and 0.68 between SAPHIR and 2A25 observations. For the same month, we find a correlation of 0.71 between 2A12 and 2A25. While comparing the statistics, it has to be borne in mind that TMI and PR have near concurrent observations (within 1 min), whereas SAPHIR may have large time differences with TMI and PR observations. Nevertheless, the SAPHIR performs very well vis-à-vis TMI and PR.

We have further presented rain from SAPHIR associated with a tropical cyclone Phailin that persisted over the Bay of Bengal from 9-12 October, 2013. This was recorded as a category 5 cyclone with a maximum wind speed of about 140 knots. Phailin made its landfall on 12 October 2013. A cyclonic system is an excellent atmospheric phenomena to critically evaluate the performance of the retrieval algorithm as several types of clouds and rain structures are present in the system. For comparison purpose, we have analysed all the available rain products over that region which are coincident with the SAPHIR. We use 3B42 available as 3-hourly averaged rain rate, 3B40-RT and GSMaP available as hourly averaged rain rates for this comparison. 3B42 (Huffman et al., 2007) is a merged product, 3B40-RT is an intermediate product of 3B42 which is derived from microwave observations only, whereas GSMaP (Aonashi et al., 2009) is a $0.1^0 X 0.1^0$ grided rain product which is available hourly. All the comparison performed here, are in $0.25^0 X 0.25^0$ rectangular grid. We calculate the rain from SAPHIR and presented in Fig 10 (a). The corresponding rain from 3B42, GSMaP and 3B42-RT are shown in Fig 10 (b), (c) and (d), respectively. Over the study area, the Megha-Tropiques has an observation time of ~2050 UTC, whereas all the other products are at 2100 UTC. From these figures we can see SAPHIR picks up the intensity and pattern of rain over the cyclonic area very well, as exhibited by other rain products. When rain rates are compared qualitatively between SAPHIR and 3B42, and between SAPHIR and GSMaP, we find correlation of 0.64 and 0.70, rmse of 1.16 and 2.24 mm/h and bias of 0.12 and 0.60 mm/h, respectively. A similar comparison of rain from GSMaP and 3B42 shows a correlation of 0.72, rmse of, 2.1 mm/h and bias 0.26 mm/h. Here, it may be to note that the discrepancies between different products are possibly due to their different observation time. Nevertheless, SAPHIR rain shows a good agreement with TRMM products.

The study presented herein provides a detail account of rain detection and measurement algorithm from SAPHIR. The algorithm is in two parts; the first part deals with rain identification, and the second provides the rain amount at identified pixels. The both procedures are developed separately for land and oceans and for each of the 182

scan positions of the SAPHIR. We have carried out extensive study to examine the worthiness of the algorithm. This is carried out first by developing a probabilistic rain identification algorithm for SAPHIR channels. We examined the effect of pixels with false rain and missing rain on rain identification. We find that their effect is limited to only very low rain regime. We further compared the rain identified by SAPHIR with TRMM-3B42 and that shows a good match at rain rates > 0.25 mm/h. It may be recalled that TRMM-3B42 is an IR-Microwave merged product and hence suppose to offer better estimate of rainfall than either of them. In the second step, we have tried to estimate rain rate at the rainy pixels. The rain measurement algorithm alone explains a correlation of 0.70, rms error of 0.81 mm/h and bias of 0.04 mm/h. Together with the rain identification procedure; it explains correlation of 0.68 with rms error of 0.45 mm/h, and bias of 0.01 mm/h. The algorithm is applied to independent SAPHIR dataset and comparison results are presented. Further, monthly rain is compared with TRMM-3B42 rain, which explains a correlation of 0.84 and standard deviation 0.09 mm/h. Furthermore, we have compared the instantaneous rain associated with Phailin cyclone from SAPHIR with other standard satellite based rain products like, GSMaP, 3B42, 3B40-RT and found SAPHIR is very well able to capture the intensity and features of intense rain also. The comparison statistics presented in this report show that the SAPHIR rain retrieval algorithm works very well for rain identification as well as for rain estimation at instantaneous, daily and monthly basis. The comparison at instantaneous basis with independent dataset (test dataset) gives us confidence that algorithm works satisfactorily.

## 4. Operational Implementation Steps

(a) We have static binary files for rain/no-rain probability over land and oceans. For given geolocation (land/ocean) and pixel-scan position, the probabilities of rain/no-rain for brightness temperature from each of the six channels are instantaneously available. These procedures are incorporated in the Fortran program. The probability values in the binary files are having 182*400*6 (are arranged in following manner:

Record =1 – probability for pixel # 1, channel S1, Tb= 1 K
Record =2 – probability for pixel # 1, channel S1, Tb= 2 K
.
.
Record =400 – probability for pixel # 1, channel S1, Tb= 400 K
Record =401 – probability for pixel # 1, channel S2, Tb= 1 K
.
.
Record =400*6 – probability for pixel # 1, channel S6, Tb= 400 K
Record =400*6+1 – probability for pixel # 2, channel S1, Tb= 1 K
.
.
Record =182*400*6(436800) – probability for pixel # 182, channel S6, Tb= 400 K

The above arrangement of records, enable us to find the probability value instantaneously for given pixel position, brightness temperature and frequency channel from the input data file. This can be calculated as follows:

$$irec=(k-1)*2400+(j-1)*400+i$$

where, irec is record number for finding the probability, k is scan position number, j is channel number and I is brightness temperature in integer. The probability values are available at each discreet integer values of the brightness temperatures. For fractional part of the brightness temperatures, the probability is calculated by linear interpolation from two adjacent integer values are performed.

(b) Once the step 1 is completed, based on probability associated with all 6 channels we find average probability of rain as $P_{RR}$ and probability of no-rain as $P_{NR}$. We then normalize them to get probability of rain ($P_R$) and probability of no-rain ($P_N$) as follows:

$$P_R = \frac{P_{RR}}{R_{RR} + P_{NR}}$$

$$P_N = \frac{P_{NR}}{R_{RR} + P_{NR}}$$

A pixel is considered as rainy if $P_R > 0.63$ over land and $> 0.6$ over oceans.

(c) Once a pixel is identified as rainy, we calculate rain from Equ. (1). The coefficients a, b and c are different for each pixel locations and surface type (land/ocean). The coasts are considered having maritime atmosphere. We have generated a static dataset of coefficients in which each row has a set of coefficients which represents the pixel location. For land a is found to be zero.

A flow-chart of these procedures a provided in Fig. 11.

## 5. Format of the output and the domain

The output is made available in the form of geolocation (latitude-longitude) and rain rate in mm h$^{-1}$. The domain is global tropics within SAPHIR coverage area over land and oceans.

## 6. Expected Accuracy

The achieved accuracy of instantaneous rain retrieval with respect to TRMM-PR is 0.91 mm/h.

On monthly scale, expected rmse with respect to TRMM 3B42 V7 is ~0.1 mm/h.

## 7. Conclusion and Future Scope

Though SAPHIR is not specifically designed for rain estimation, yet it is shown for its use for rain identification as well as for rain estimation. The best instrument on MT for rain estimation is MADRAS but it has already been declared as non-operational due to problem with its scanning mechanism. In the absence of MADRAS observations, SAPHIR measurements can serve as supplementary to MADRAS measurements for rain measurement to fulfill the science objectives of the MT mission. The SAPHIR based rain identification may even help flagging off the humidity profile measurements by it. The rain measurement from SAPHIR opens up opportunity for measuring rain from similar channels available on other satellite missions. In future, there is also possibility to combine SAPHIR measurements with thermal IR measurements from another instrument, ScaRaB, on Megha-Tropiques for more accurate rain measurement.

## 8. Acknowledgement

## References

Anonymous, 2011, Tropical Rainfall Measuring Mission (TRMM) Precipitation Radar Algorithm, Instruction Manual for Version 7, Published by TRMM Precipitation Radar Team, Japan Aerospace Exploration Agency (JAXA), and National Aeronautics and Space Administration (NASA), (available at: http://www.eorc.jaxa.jp/TRMM/documents/PR_algorithm_product_information/pr_manual/PR_Instruction_Manual_V7_L1.pdf), p 170.

Aonashi K., Awaka J., Hirose M., Kozu T., Liu G., Shinge S., Kida S., Seto S., Takahashi N., and Takayabu Y. N., 2009, GSMaP passive microwave precipitation retrieval algorithm: Algorithm description and validation. *J. Metror. Soc. Japan*, **87A**, 119-136.

Awaka, J., T. Iguchi, H. Kumagai, and K. Okamoto, 1997, Rain type classification lgorithm for TRMM precipitation radar. *Proc. IEEE Int. Conf. on Geoscience and Remote Sensing (IGARSS-97)—A Scientific Vision for Sustainable Development*, **4**, IEEE, 1633–1635.

Bennartz, R., and P. Bauer, 2003, Sensitivity of microwave radiances at 85 –183 GHz to precipitating ice particles, *Radio Science*, **38(4)**, 8075, doi:10.1029/2002RS002626.

Buehler, S. A., M. Kuvatov, and V. O. John, 2005, Scan asymmetries in AMSU-B Data, *Geophys. Res. Lett.*, **32**, L24810, doi:10.1029/2005GL024747.

Burns, B. A., X. Wu, and G. R. Diak (1997), Effects of precipitation and cloud ice on brightness temperatures in AMSU moisture channels, *IEEE Transactions on Geosciences and Remote Sensing*, **35**, 1429–1437.

Eymard, L., M. Gheudin, P. Laborie, F. Sirou, C. Le Gac, J.P. Vinson, S. Franquet, M. Desbois, R. Roca, N. Scott, P. Waldteufel, 2001, The SAPHIR humidity sounder, MEGHA-TROPIQUES 2nd Scientific Workshop, 2-6 July 2001, Paris, France. (available at: http://meghatropiques.ipsl.polytechnique.fr/submit-a-document/2nd-workshop/the-saphir-instrument-on-megha-tropiques/download.html)

Gairola, R M, C Mahesh, and Varma A K, 2011, Operational software for retrieval of precipitation from Megha-Tropiques- MADRAS, Internal report No. SAC/EPSA/AOSG/MT-UP/TR/64/June/2011.

Gohil, B S, R M Gairola, A K Mathur, A K Varma, C Mahesh, R K Gangwar and P K Pal, 2013, Algorithms for retrieval of Geophysical Parameters from MADRAS and SAPHIR sensors of Megha-Tropiques Satellite – Indian Scenario, *Quarterly Journal of Royal Meteorological Society*, **139**, 954–963.

Hilburn, K. A., and F. J. Wentz, 2008, Intercalibrated passive microwave rain products from the Unified Microwave Ocean Retrieval Algorithm (UMORA) *Journal of Applied Meteorology and Climatology*, **47**, 778-794.

Hong, G., G. Heygster, J. Miao, and K. Kunzi, 2005, Sensitivity of microwave brightness temperatures to hydrometeors in a tropical deep convective cloud system at 89–190 GHz, *Radio Science*, **40**, RS4003, doi:10.1029/2004RS003129.

Huffman, G. J., R. F. Adler, D. T. Bolvin, G. Gu, E. J. Nelkin, K. P. Bowman, Y. Hong, E. F. Stocker, and D. B. Wolff, 2007, The TRMM multi-satellite precipitation analysis: Quasi-global, multi-year, combined-sensor precipitation estimates at fine scale, *Journal of Hydrometeorology*, **8**, 38–55, doi: http://dx.doi.org/10.1175/JHM560.1

Kawamoto K. and K Suzuki, 2013, Comparison of water cloud microphysics over mid-latitude land and ocean using CloudSat and MODIS observations *Journal of Quantitative Spectroscopy and Radiative Transfer*, **122**, pp.13-24; 2013, 10.1016/j.jqsrt.2012.12.013.

Kummerow, C., W. Barnes, T. Kozu, J. Shiue, and J. Simpson, 1998, The Tropical Rainfall Measuring Mission (TRMM) sensor package, *Journal of Atmospheric and Oceanic Technology*, **15**, 809–816, doi:10.1175/1520-0426.

Liu, G.,1998, A fast and accurate model for microwave radiance calculations. *J. Meteor. Soc. Japan*, **76**, 335–343.

Liu, G., and J. A. Curry, 1999, Tropical ice water amount and its relations to other atmospheric hydrological parameters as inferred from satellite data, *Journal of Atmospheric Sciences*, **38**, 1182–1194.

Mathur, A. K., R.K. Gangwar, B.S. Gohil, S.K. Deb, P. Kumar, M. V. Shukla, B. Simon, and P. K. Pal, 2013, *Current Science*, **104** (12), 1650-1655.

Muller, B. M., H. E. Fuelberg, and X. Xiang, 1994, Simulations of the effects of water vapor, cloud liquid water, and ice on AMSU moisture channel brightness temperatures, *Journal of Applied Meteorology*, **33**, 1133–1154.

Piyush, D N, A K Varma, P K Pal and G Liu, 2012, An Analysis of Rainfall Measurements over Different Spatio-Temporal Scales and Potential Implications for Uncertainty in Satellite Data Validation, *Journal of Meteorological Society of Japan*, **90** (4), doi: 10.2151/JMSJ.2012-408.

Rudolf, B, 1995, Global Precipitation Climatology Centre; In WMO/UNEP, The global climate system review, climate system monitoring June 1991 – November 1993, WMO No. 891, Genf, 37.

Varma, A K and P K Pal, 2012, Use of TRMM Precipitation Radar to address the problem of rain detection in Passive Microwave Measurements, *Indian Journal of Radio and Space Physics*, **41** 411-420.

Varma, A. K. and G. Liu, 2010, On Classifying Rain Types Using Satellite Microwave Observations, *Journal of Geophysical Research*, 115, D07204, doi:10.1029/2009JD012058.

Varma, A. K., and G. Liu, 2006, Small-Scale Horizontal Rainrate Variability by Satellite, *Monthly Weather Review*, 134 (10), 2722-2733.

Varma, A. K., G. Liu, and Y. J., Noh, 2004, Sub-Pixel Scale Variability of Rainfall and Its Application to Mitigate the Beam-Filling Problem, *Journal of Geophysical Research*, 109, D18210, doi:10.1029/2004JD004968.

Varma A K, R M Gairola and B S Gohil, 2011, Operational software for retrieval of cloud liquid water, integrated water vapour and wind speed over global oceans from Megha-Tropiques- MADRAS, Internal report No. SAC/EPSA/AOSG/MT-UP/TR/65/June/2011.

**Table 1:** Specifications of MADRAS Channels

| Channel | Frequency (GHz) | Polarization | NE$\Delta$T (K) | Spatial Resolution (Km) |
|---------|-----------------|--------------|-----------------|-------------------------|
| M1 | 18.7 | H+V | 0.7 | 40 |
| M2 | 23.8 | V | 0.7 | 40 |
| M3 | 36.5 | H + V | 0.7 | 40 |
| M4 | 89 | H + V | 1.0 | 10 |
| M5 | 157 | H + V | 2.6 | 6 |

**Table 2**: Specifications of SAPHIR Microwave Sounder

| Channel | Center Frequency (GHz) | Max. Passband (MHz) | $\Delta$T (K) Sensitivity at 300 K | Absolute Calibration (K) Over 180 - 300K | Pol. |
|---------|------------------------|---------------------|------------------------------------|------------------------------------------|------|
| $S_1$ | 183.31 ± 0.2 | 200 | 1/2 | ± 1 | H |
| $S_2$ | 183.31 ± 1.1 | 350 | 0.7/1.5 | ± 1 | H |
| $S_3$ | 183.31 ± 2.8 | 500 | 0.7/1.5 | ± 1 | H |
| $S_4$ | 183.31 ± 4.2 | 700 | 0.6/1.3 | ± 1 | H |
| $S_5$ | 183.31 ± 6.8 | 1200 | 0.6/1.3 | ± 1 | H |
| $S_6$ | 183.31 ± 11.0 | 2000 | 0.5/1.0 | ± 1 | H |
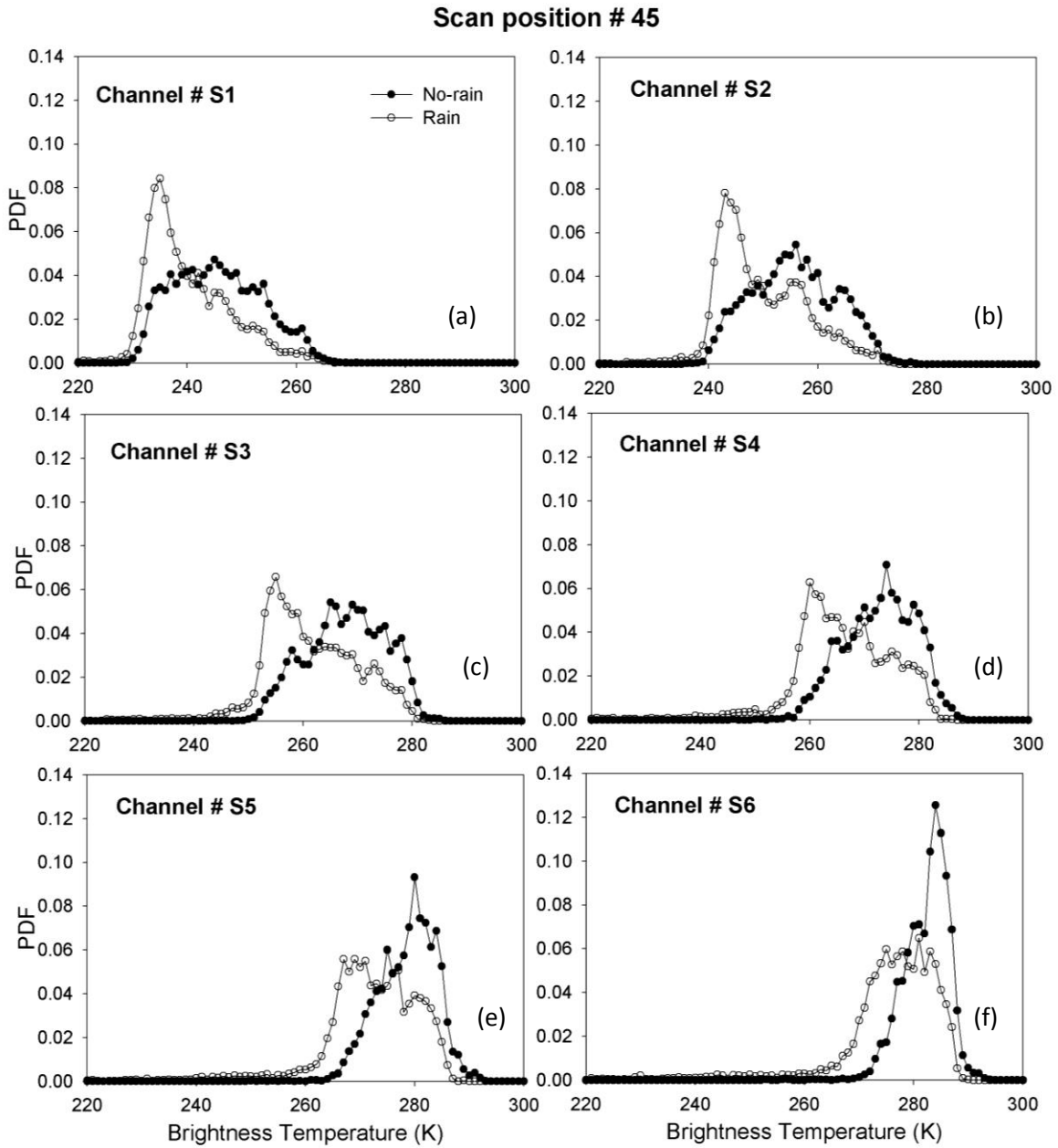
**Fig. 1:** PDFs of SAPHIR brightness temperatures for a typical scan position # 45 for rainy (line joining open circles) and non-rainy (line joining solid circles) conditions over oceans for channel (a) S1 (b) S2 (c) S3 (d) S4 (e) S5 and (f) S6.
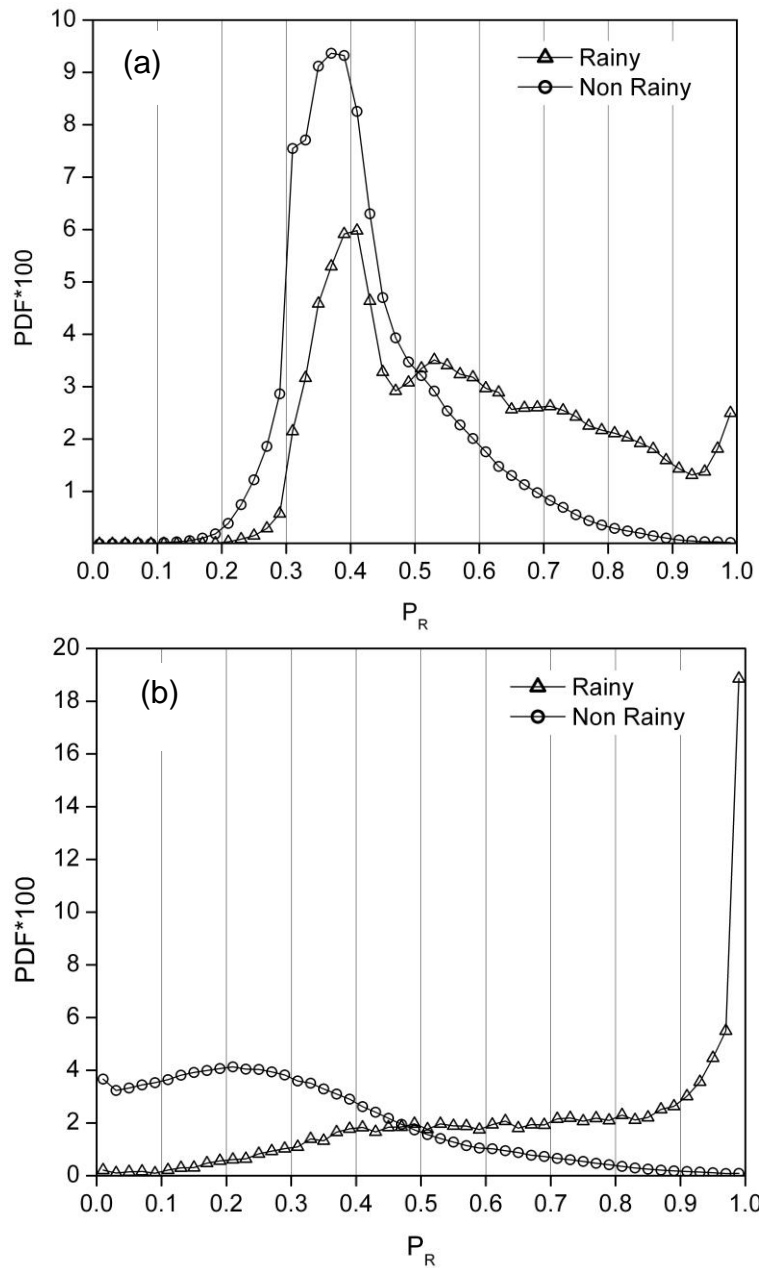
**Fig. 2:** Distribution of $P_R$ for rainy (line joining open triangles) and non-rainy (line joining open circles) over (a) ocean and (b) land, from training datasets for all pixel locations.
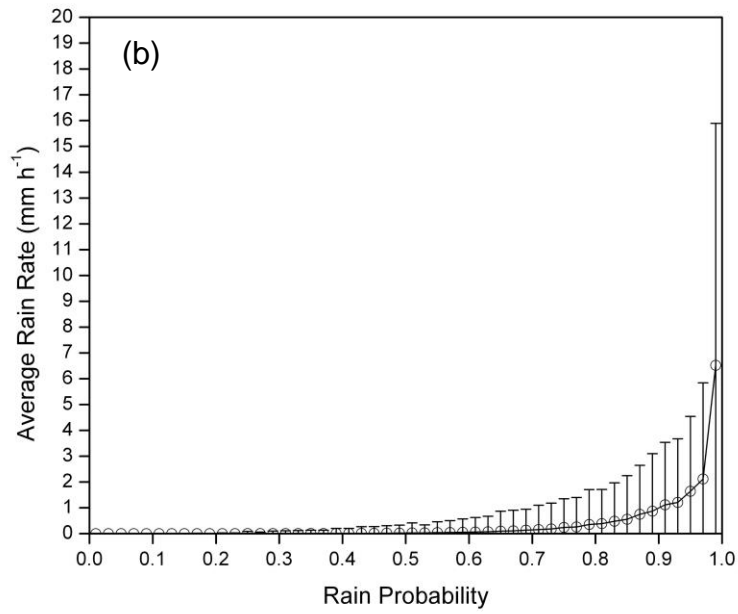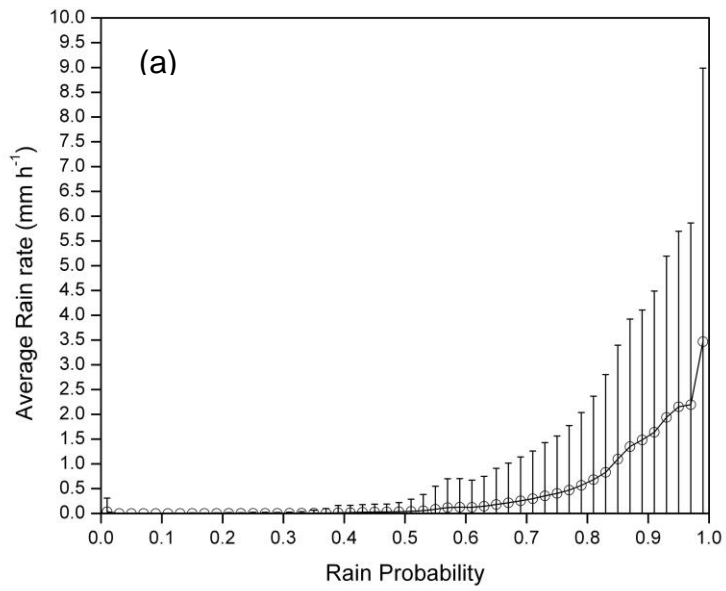
**Fig. 3:** Average rain rate (mm/h) with vertical bars of Standard Deviation (SD) as a function of $P_R$ from the rainy dataset over (a) oceans and (b) land.
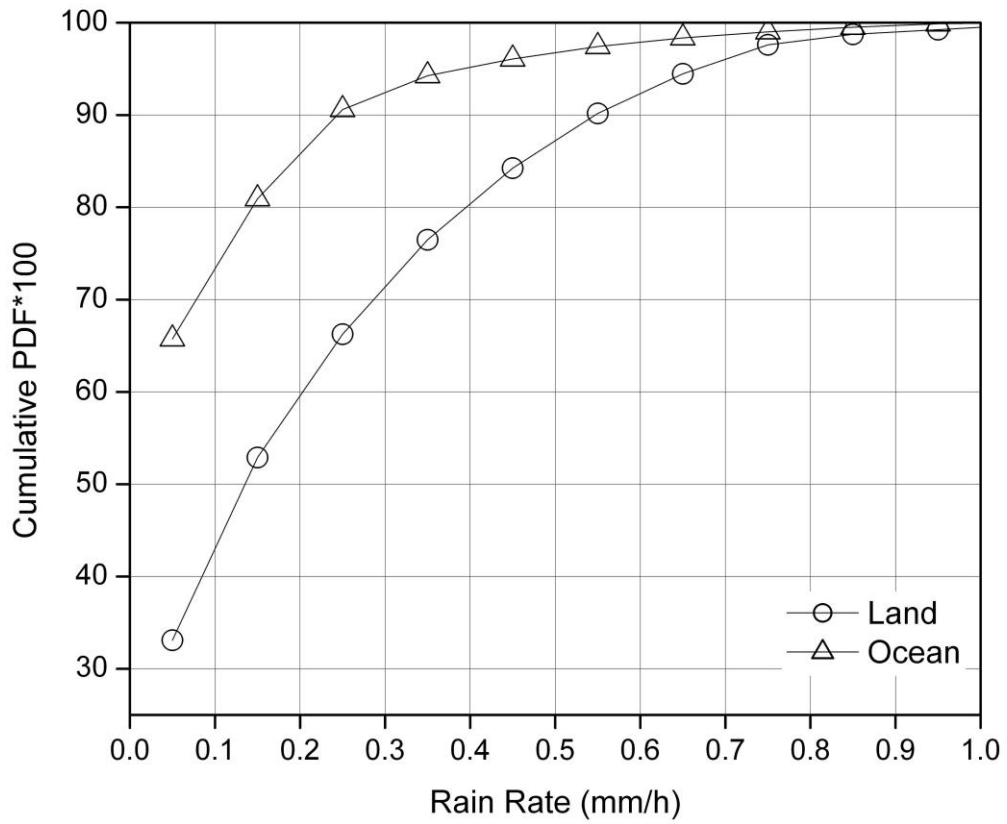
**Fig. 4:** Cumulative Probability Distribution of rain rates from the non-rainy points that turn rainy with (a) $P_R > 0.6$ for Ocean (open triangle) and (b) $P_R > 0.63$ for Land (open circle).
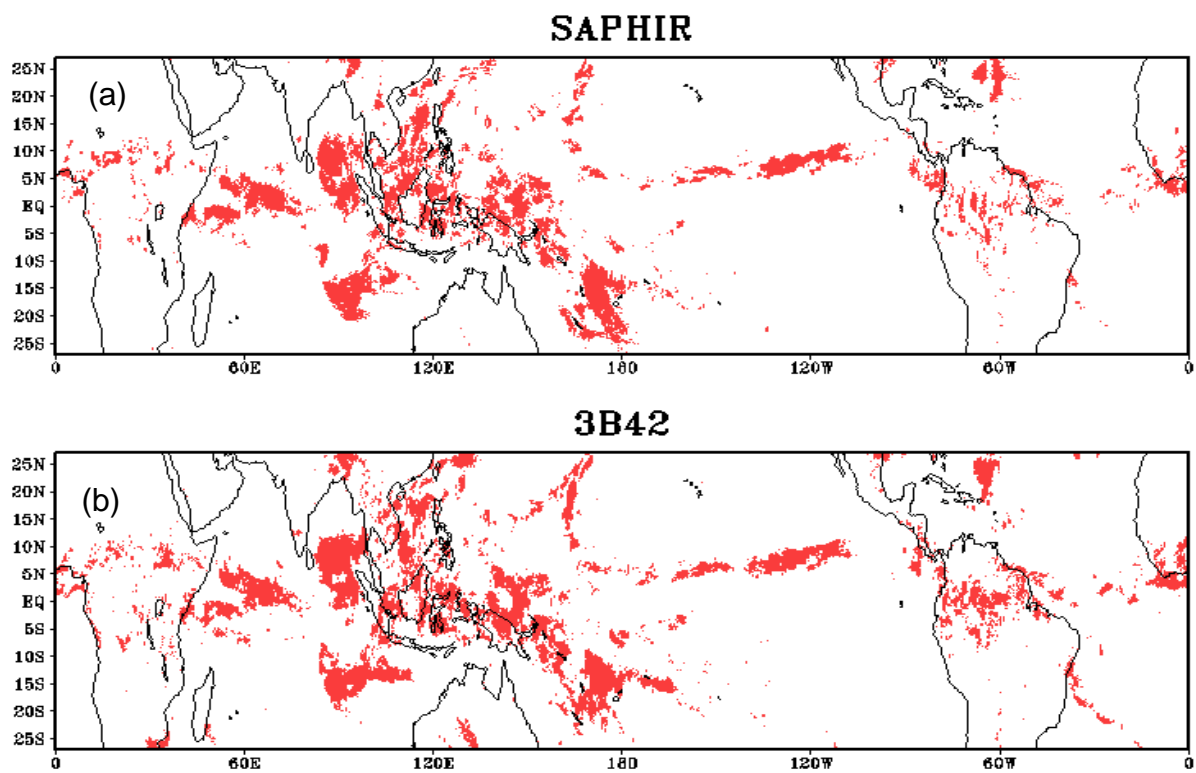
**Fig. 5:** Rain/No-rain map for a typical day of 11 May 2013 for (a) 3B42 and (b) SAPHIR, for rain rate > 0.25 mm/h.
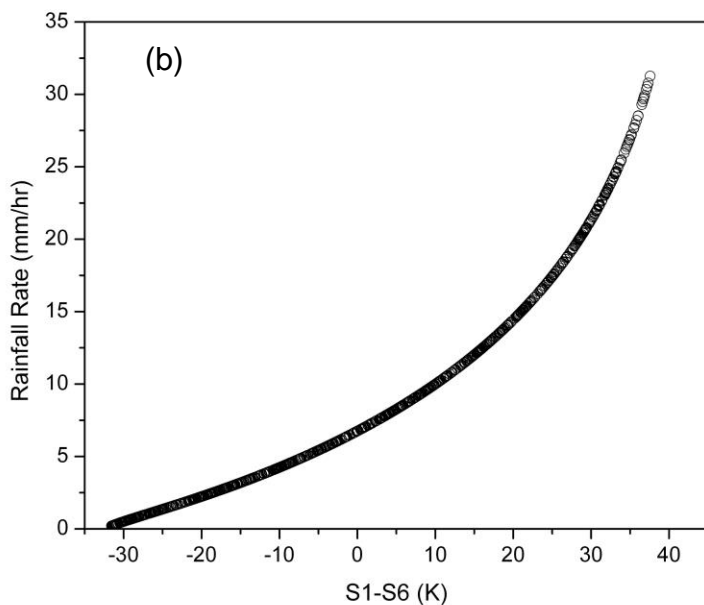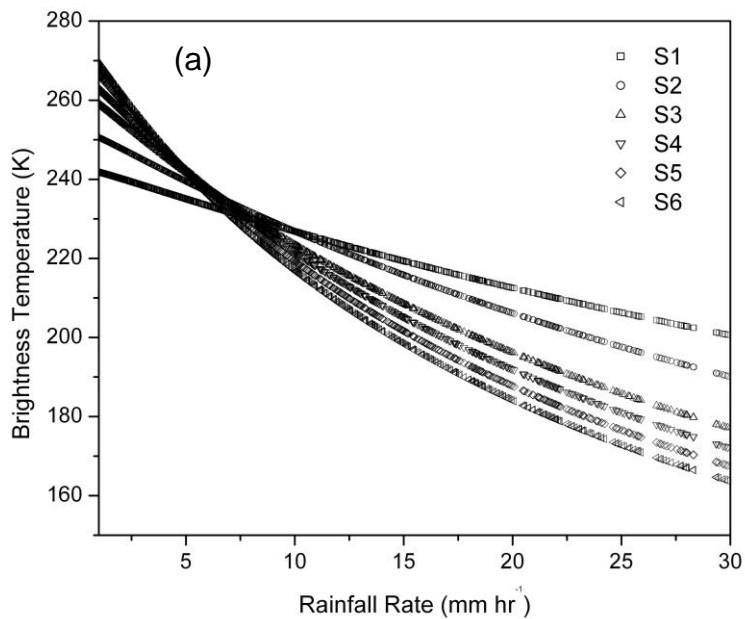
**Fig. 6:** (a) Depression in brightness temperature with increasing rain rates for all the six SAPHIR channels, (b) variation of brightness temperature difference from SAPHIR (S1-S6) with surface rain.
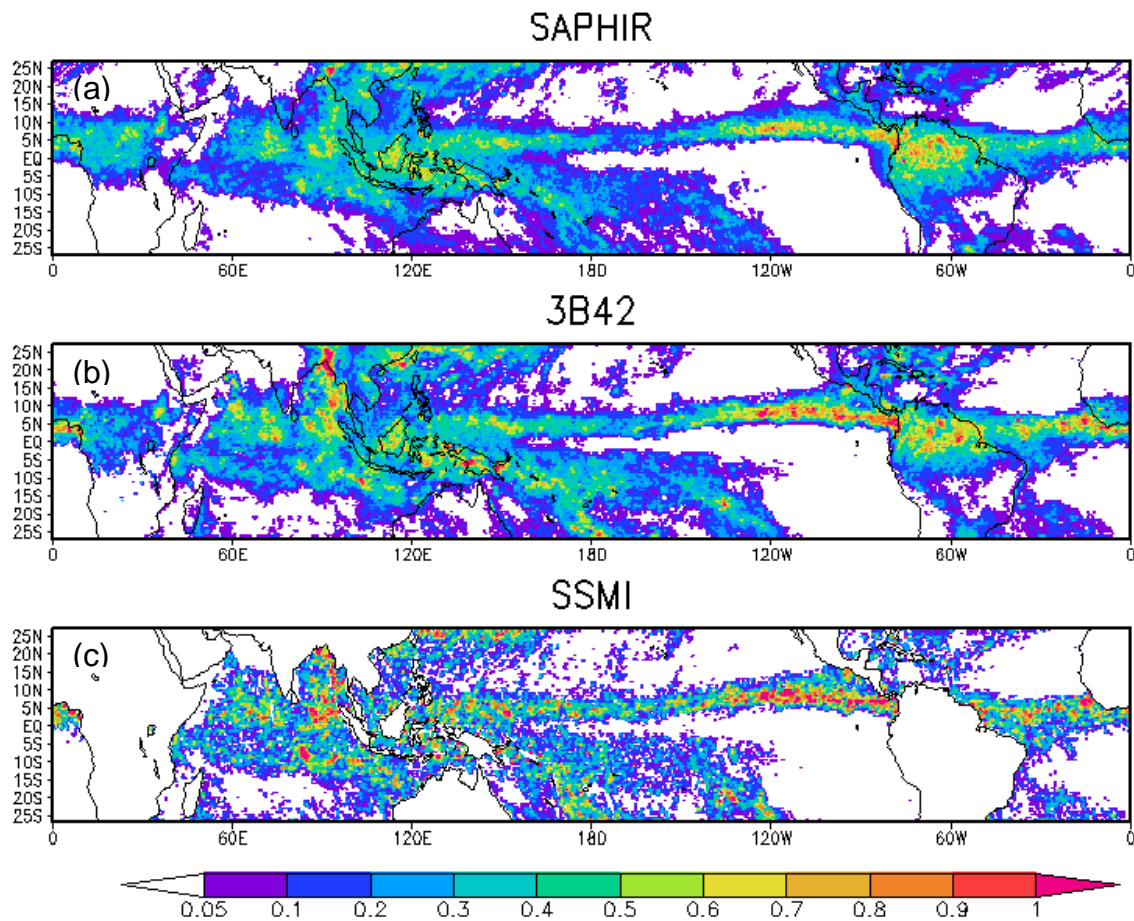
**Fig. 7:** Monthly averaged gridded (0.25°X0.25°) rain rates (mm/h) from (a) SAPHIR, (b) TRMM-3B42 and (c) SSMIS, for the month of May, 2013. The rain from SSMIS is only over oceans.
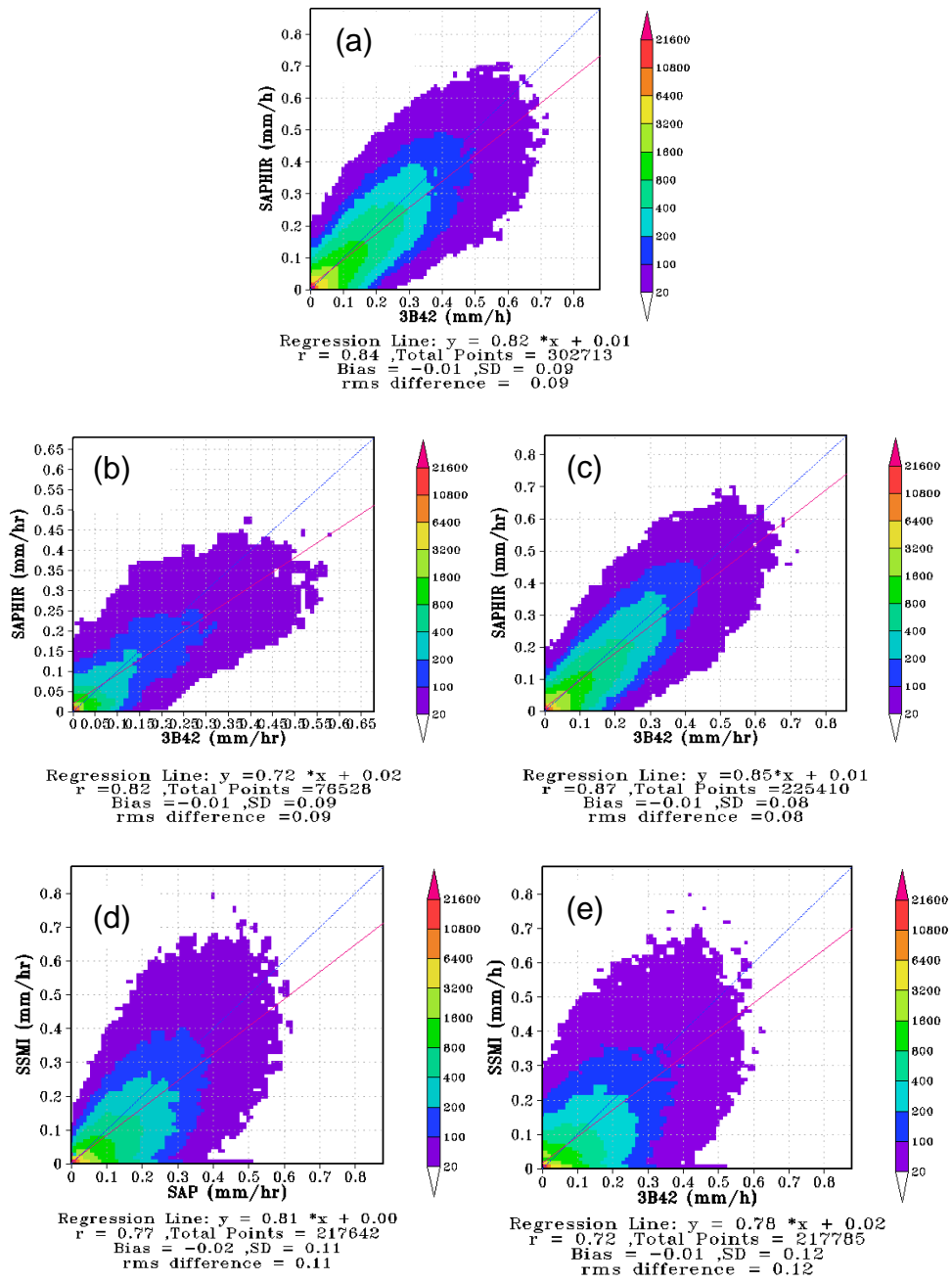
**Fig. 8:** Comparison of monthly gridded rain maps (from Fig. 6) between (a) SAPHIR and 3B42 over all regions, (b)  over land, (c) over oceans, (d) SAPHIR and SSMIS over oceans, and (e) SSMIS and 3B42 over oceans.
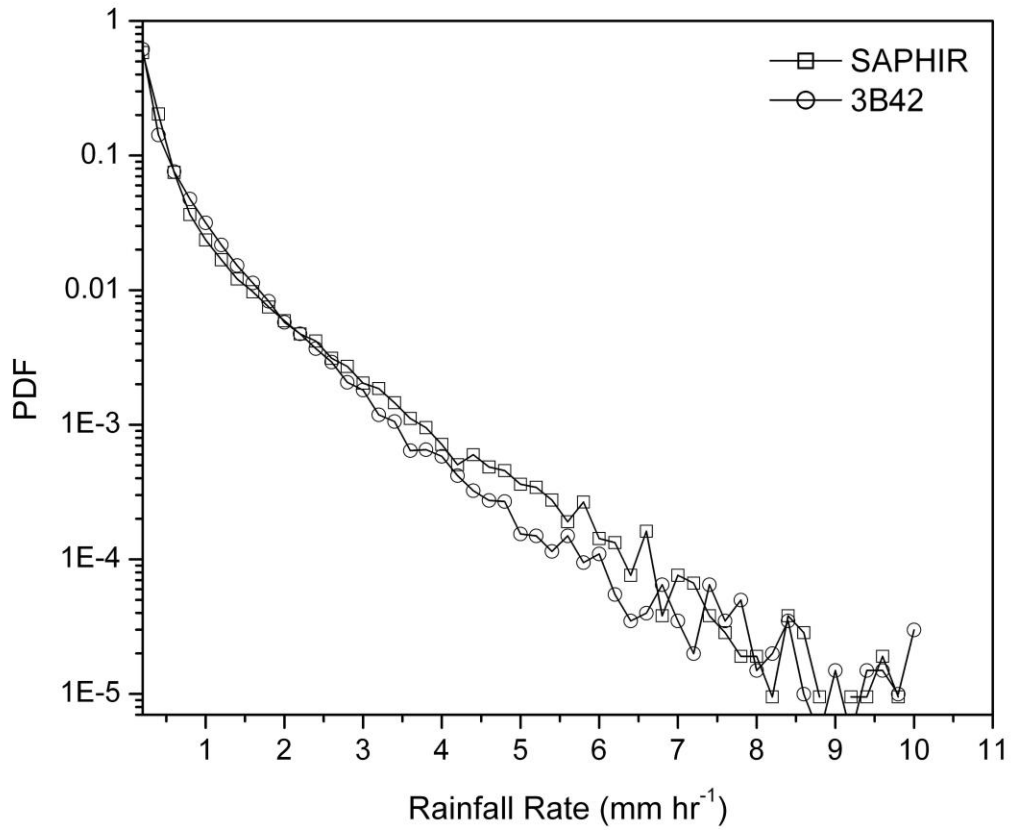
**Figure 9:** PDF of averaged daily rain rate (mm/h) from SAPHIR and TRMM-3B42 for May 2013
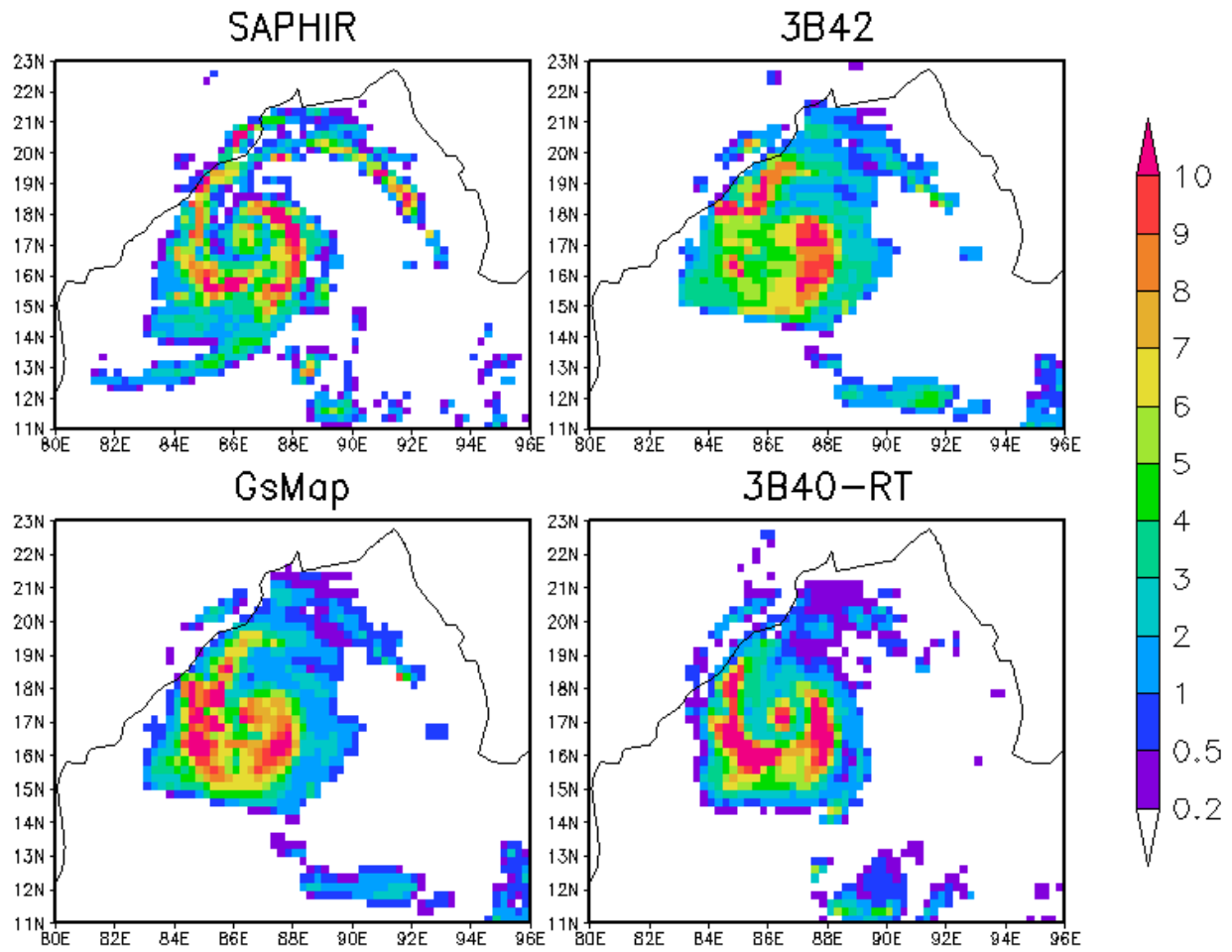
**Fig. 10:** Distribution of rain rates (mm/hr) from (a) SAPHIR, (b) 3B42 (c) GSMaP (d) 3B40-RT , over a tropical cyclone Phailin on 11 October, 2013 arround 2100 UTC.
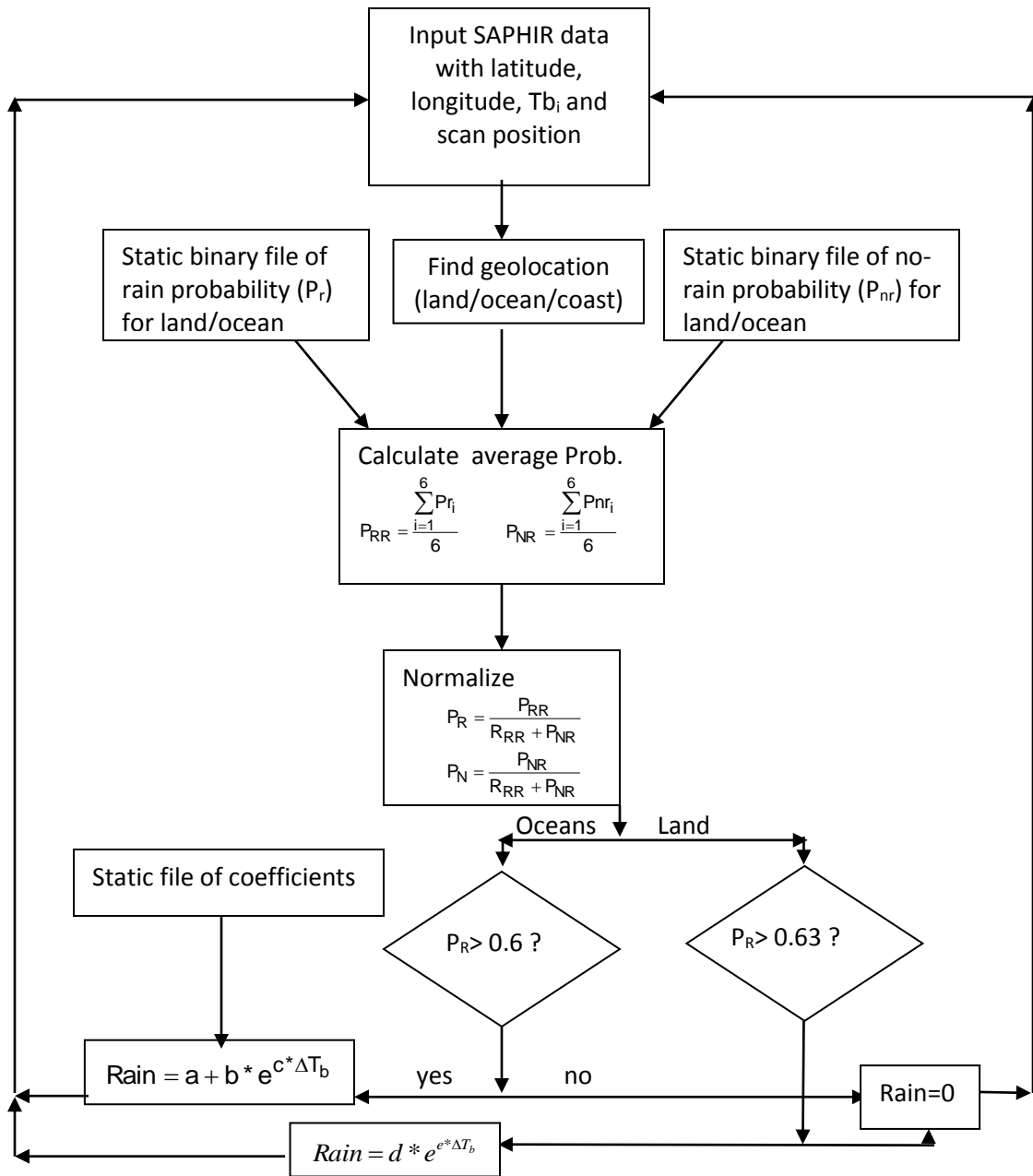
**Fig.11:** Flow chart of rain estimation from SAPHIR.